

pubs.acs.org/journal/apchd5 Letter

# Tuning Plasmonic Coupling from Capacitive to Conductive Regimes via Atomic Control of Dielectric Spacing

Sharmin Haq,<sup>§</sup> Tefera E. Tesema,<sup>§</sup> Bisweswar Patra, Eric Gomez, and Terefe G. Habteyes\*



Cite This: ACS Photonics 2020, 7, 622–629



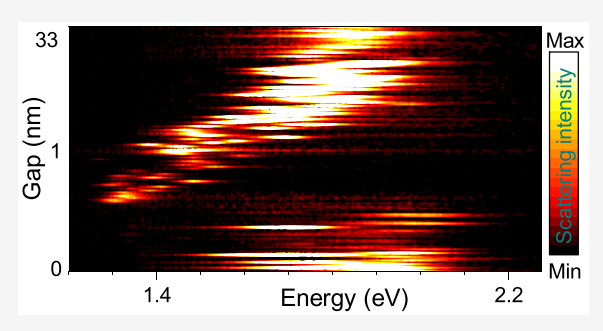
**ACCESS** 

Metrics & More

Article Recommendations

Supporting Information

ABSTRACT: The gap length between plasmonic nanoparticles determines the strength of the optical coupling that results in electromagnetic field enhancement for spectroscopic and other applications. Although gap plasmon resonances have been the focus of increasing research interest, experimental observations have primarily been limited to the coupling of spherical nanoparticles that may not provide clear spectral contrast of the optical response as the interaction evolves from capacitive to charge transfer with the gap size decreasing to sub-nanometer. Here, by taking advantage of the sharp plasmon resonances of colloidal gold nanorods coupled to gold film, we present the spectral evolution of gap plasmon resonance as the particle—film spacing varies from over 30 nm to the



touching limit. We find that the capacitive gap plasmon resonance of the coupled system red-shifts and narrows continuously until it vanishes at the quantum tunneling limit, in contrast to the nonlocal and Landau damping effects that are expected to result in relative blue-shifting and spectral broadening. When the spacer thickness is further decreased, high order cavity modes appear, and eventually single peak broad resonances that are characteristic of tunneling and direct contact particle—film interaction emerge. The experimental observations show that nanorods are better suited for creating cavity plasmon resonances with high quality factor, and the spectral contrast at the transition provides clarity to develop improved theoretical modeling of optical coupling at sub-nanometer gap lengths.

KEYWORDS: particle on metal film, plasmon coupling, cavity modes, charge transfer, tunneling, gold nanorods, atomic layer deposition

surface plasmon field enhancement that is large enough A for single molecule detection can be obtained when two or more resonant plasmonic metal nanoparticles are coupled through dipole-dipole and higher order mode interactions.<sup>1,2</sup> According to classical electromagnetic (CEM) theory, the plasmon resonance energy of the coupled system continuously shifts to the red, and the field enhancement in the gap between the particles increases exponentially as the gap length decreases to sub-nanometer scale.3 However, recent theoretical4-6 and experimental<sup>7-10</sup> advances indicate that CEM theory overestimates the energy shift and the field enhancement as the gap size decreases to a nanometer and sub-nanometer regimes. Electron tunneling,<sup>4</sup> nonlocal effect,<sup>12</sup> and Landau damping<sup>13</sup> have been proposed as possible mechanisms that contribute to the deviation from the CEM simulation that uses the dielectric function of the bulk metal as an input. Various experimental approaches have been implemented to achieve sub-nanometer gap lengths. Savage et al. used electrostatic force and piezoelectric actuation stages to bring the tip-to-tip gap between two ball-type Au-coated atomic force microscope tips within the tunneling regime. Scholl et al. used the electron beam of a transmission electron microscope to manipulate the gap length in dimers of silver nanospheres, while monitoring the plasmonic optical response using electron energy-loss spectroscopy.9 The classic experimental results of

Savage et al.<sup>7</sup> and Scholl et al.<sup>9</sup> appear to indicate smooth transition of the plasmonic response when the gap length between the spherical nanoparticles varies from a nanometer to a tunneling and touching limit.

Placing plasmonic metal nanoparticles on metal film has been used as a more convenient approach for investigating plasmon coupling with accurate control of the gap size. <sup>8,14</sup> In this particle-on-film configuration, the dipole—image dipole interaction as a function of particle—film separation mimics the dipole—dipole interaction between two nanoparticles. <sup>15</sup> For particle—film coupling, the gap distance can be controlled conveniently by depositing a spacer layer on the film prior to placing the nanoparticle using different materials including self-assembled thiol molecules, <sup>8,16</sup> graphene, <sup>17,18</sup> DNA origami, <sup>19</sup> and atomic layer deposition (ALD) of aluminum oxide. <sup>20,21</sup> Particle-on-film plasmonic systems have been used for studying molecular conductance, <sup>22,23</sup> single molecule detection, <sup>24–26</sup>

Received: February 11, 2020 Published: February 19, 2020

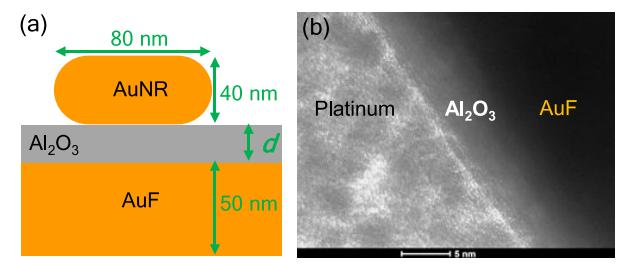


and electron nonlocal screening effects<sup>8</sup> as well as for other interesting studies of optical properties and applications.<sup>27–35</sup>

In this work, a nanoparticle-on-film configuration is implemented by coupling colloidal gold nanorods (AuNRs) to gold film (AuF). The choice of AuNRs, as opposed to nanospheres that have been used as the classic model system in the investigation of nonlocal effect<sup>8</sup> and quantum tunneling,<sup>7,5</sup> is critical for revealing the nature of the coupling interaction at sub-nanometer separation distances. First, the inherently much narrower resonances of AuNRs than those of gold spheres<sup>36</sup> are desirable to probe the plasmonic responses of the coupled system with higher sensitivity, particularly at the tunneling limit. Second, for AuNRs coupled to AuF, the plasmon resonance peak energy shifts from red to near-infrared with decreasing gap and then jumps to the charge transfer plasmon resonance that peaks at  $\sim 1.8$  eV at the touching limit.<sup>37</sup> This spectral contrast is critical in understanding the transition of the coupling interaction from capacitive to charge transfer as the gap length decreases to the touching limit. In addition, as it will be shown, the excitation of cavity resonances of gold nanorods on metal film is more efficient for the in-plane polarized excitation field than for the out-of-plane polarization that is required for inducing dipole-image dipole interaction that couples the excitation of spherical particles to metal film.

By taking advantage of the desirable optical properties of AuNRs coupled to AuF, we show the evolution of gap plasmon resonances as the gap length varies from over 30 nm to the touching limit, providing a complete picture for understanding the coupling properties. We observe that, with the gap size decreasing to the tunneling limit, the peak energy shifts to the red continuously, shifting from 1.87  $\pm$  0.06 eV at 33 nm to  $1.32 \pm 0.03$  eV at the tunneling limit. The resonance energy shift is accompanied by significant narrowing of the spectral linewidth, decreasing from 151  $\pm$  27 to 49.0  $\pm$  0.6 meV. Interestingly, the spectral red-shifting and narrowing appear to be accelerated as the gap length approaches the quantum tunneling limit, which is in contrast to quantum mechanical tunneling and Landau damping effects. When the gap size is further decreased by reducing the oxide thickness, high order cavity modes start to appear, gradually converging to a single peak resonance that is characteristic of tunneling and direct contact interaction between the gold nanorod and the gold film.3

The AuNR-AuF coupling geometry is shown by the schematic in Figure 1a. The procedure for creating the aluminum oxide film using ALD as well as the optical measurement is provided in the Supporting Information. The oxide film is deposited on e-beam evaporated Au film (~50 nm gold/2 nm Ti/silicon) by pulsing trimethylaluminum and water vapors alternately in N2 carrier gas using the Picosun ALD system at 150 and 200 sccm flow rates, respectively. The optimal growth temperature (100 °C) is determined based on morphological and optical analyses of the film using atomic force microscopy and variable angle spectroscopic ellipsometry (VASE), and the oxide thickness d is varied by changing the ALD cycle numbers. A representative cross-sectional transmission electron microscope (TEM) image in Figure 1b shows the thickness of the oxide layer on the AuF for 55 ALD cycles. The thickness determined using VASE is in good agreement with the corresponding value obtained using TEM as shown in Figure 1c. Hence, for a broad range of ALD cycles, the thickness is determined using VASE. Based on the slope of a linear equation fitted to the data, the growth rate is estimated



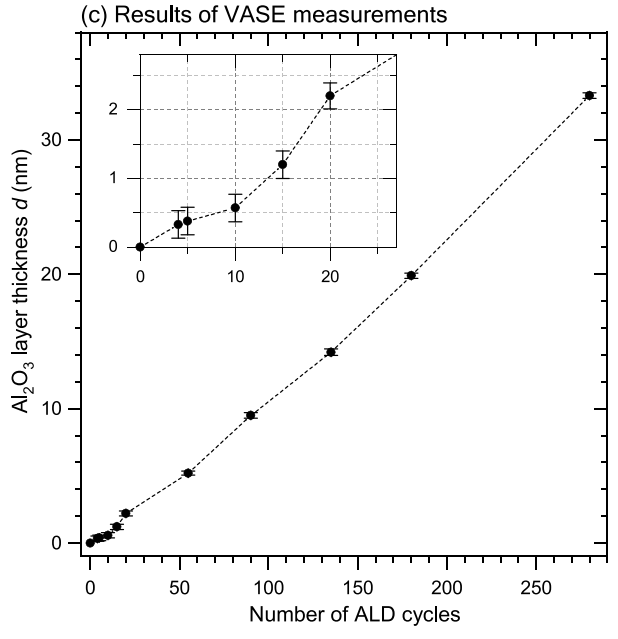
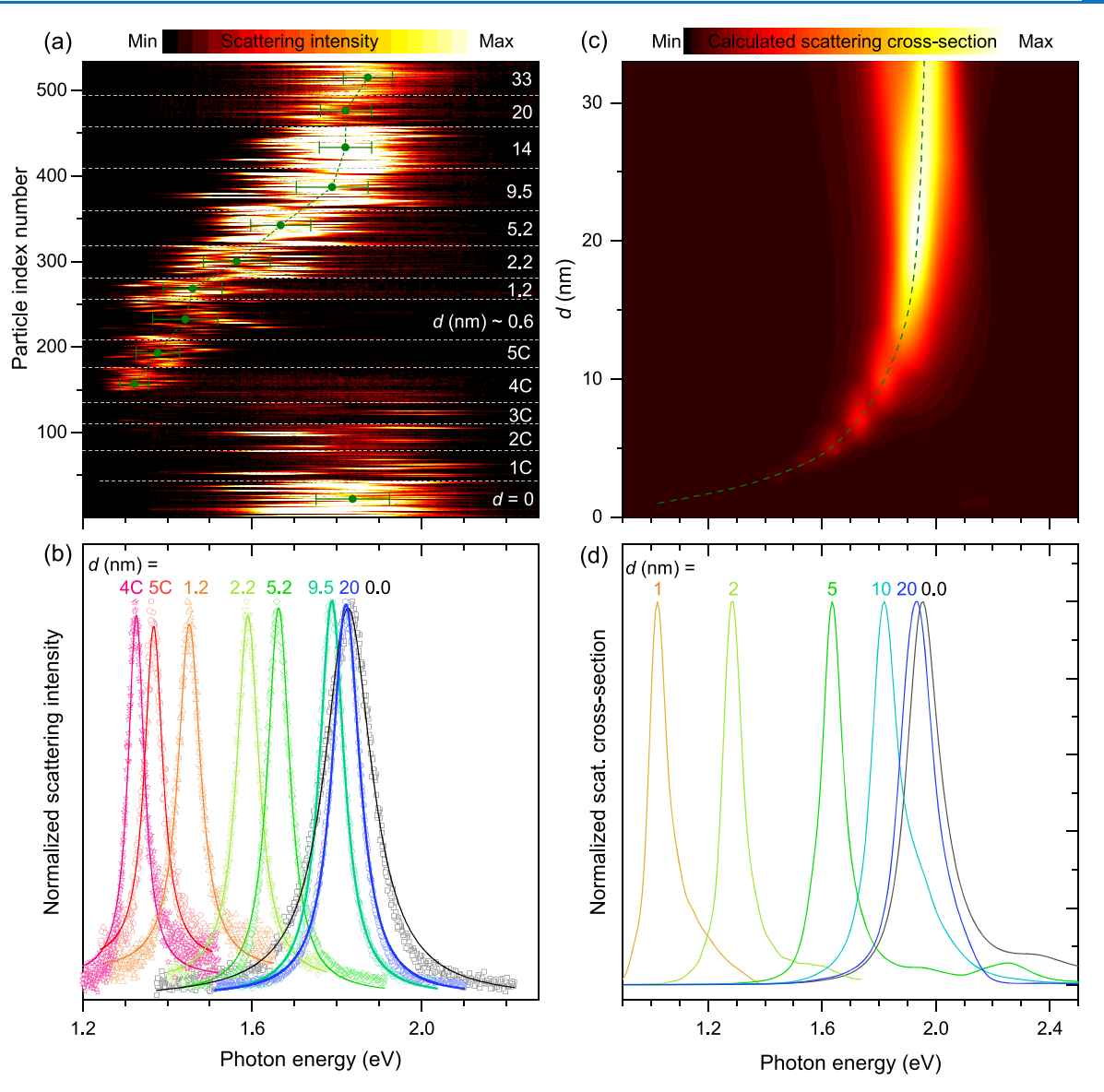


Figure 1. (a) Schematic showing the coupling of a gold nanorod (AuNR) to gold film (AuF) through aluminum oxide dielectric spacer layer of thickness d that is controlled using atomic layer deposition (ALD). (b) Representative TEM image showing the oxide thickness formed using 55 ALD cycles. The scale bar is 5 nm. (c) Oxide thickness as a function of the number of ALD growth cycles. The error bars indicate the fitting error in determining the thicknesses using the VASE procedure, and the linear trend is indicative of the fabrication reproducibility. The deviation of the thicknesses from fabrication to fabrication is within the fitting error bars.

as 1.2 Å per cycle for 20–280 cycles, and 1.63 Å per cycle for 10–20 cycles. These growth rates are in good agreement with reported growth rates on silver (0.98 Å per cycle for 30–425 cycles and 1.65 Å per cycle for 0–20 cycles). However, for ALD cycles smaller than 10, the oxide growth rate on gold film appears slower, although it is difficult to determine the thicknesses reliably using ellipsometry. The slower rate for fewer than 10 cycles may indicate inhibition of growth during the initial few cycles, and may result in nonuniform oxide film thickness. For ten cycles, the oxide spacer thickness can be estimated as ~0.6 nm, and in order to achieve continuous variation of smaller gap sizes, the ALD growth cycles have been decreased one-by-one starting at five cycles.

The optical properties of the AuNR–AuF plasmonic system are studied by measuring the dark-field scattering spectra of individual AuNRs (see Figure S1) at different aluminum oxide spacer thickness *d*, ranging from 33 nm to direct contact limit. The sample is excited by focusing unpolarized white light using a dark-field objective with numerical aperture of 0.9. The high focusing angle results in excitation field projections parallel and perpendicular to the sample plane, possibly resulting in the



**Figure 2.** Optical responses of AuNRs coupled to AuF through the aluminum oxide spacer of different thicknesses (d). (a) Intensity map representing 534 spectra of individual AuNRs for d = 33 nm to d = 0 (no ALD layer) as labeled on the right side on the plot. The labels 1C-5C on the plot indicate the number of ALD cycles. (b) Single particle dark-field scattering spectra that represent the average characteristics for the different thicknesses of the spacer layer. (c, d) Scattering cross-section calculated using the finite difference time domain method of electromagnetic simulation.

excitation of both the longitudinal and transverse modes of the AuNR as illustrated in Figure S2. There are two mechanisms that should be considered to understand the AuNR–AuF optical coupling: dipole–image dipole interaction and cavity mode excitation. For the AuNR dipole that is parallel to the film, the dipole and the image dipoles cancel out due to their antiparallel orientation. However, the excitation field oriented along the long axis of the AuNR excites the cavity mode effectively as demonstrated in the finite-difference time-domain (FDTD) simulation results (Figures S2 and S3), presumably because of high reflection coefficients of surface plasmon polaritons at the ends of the gold nanorod. Phe cavity mode can hybridize with the fundamental longitudinal mode of the AuNR, resulting in the intense field localization in the gap region as shown in Figure S3.

The evolution of the cavity resonance as a function of dielectric spacer thickness is studied by recording 25-50 spectra that represent different AuNRs for each spacer

thickness. The intensity map in Figure 2a represents 534 spectra, and it shows the variation of the plasmon resonance as d decreases from 33 nm to zero. For d = 33 nm to five ALD cycles (5C), the scattering spectra is dominated by single peaks that have Lorentzian shapes, and the average peak position shifts to red due to the increasing strength of capacitive coupling with decreasing gap size. Starting at 4C, the scattering spectra start to change drastically as shown in Figure 2a. First, broad resonances with very weak scattering intensity start to appear, and upon decreasing the gap length further by reducing the cycle numbers, multipeak resonances becomes apparent. The normalized representative single particle spectra in Figure 2b show the spectral evolution with decreasing aluminum oxide layer thickness up to 4C. The results of the electromagnetic simulation carried out using FDTD reproduces the overall trend of the observation qualitatively for  $d \ge 1$  nm as shown in Figure 2c,d. Next, we discuss the evolution of the

cavity resonances based on the average values of peak energy and linewidth.

# ■ SPECTRAL RED-SHIFTING AND NARROWING UNTIL VANISHING

In Figure 2b, single particle spectra that are representative of the average spectral characteristics at different spacer layer thicknesses are presented. The plasmon resonance peak energies and linewidths extracted from the scattering spectra by fitting the Lorentzian function to the data are plotted in Figure 3a. With d decreasing from 33 nm to the thickness obtained at 4C, the average peak energy shifts from  $1.87 \pm 0.06$  to  $1.32 \pm 0.03$  eV, and the linewidth decreases from  $151 \pm 27$  to  $49.0 \pm 0.6$  meV as shown in Figure 3a. In Figure 3b,c, the average resonance energy and linewidth are plotted as a function of d (the same data are plotted in Figure S8 in log scale). Clearly, as can be seen in Figures 2a,b and 3c, the resonance energy continuously shifts to the red until the sharp gap plasmon resonances vanish apparently at the tunneling limit.

The experimental and calculated peak energies are compared in Figure 3c. At large gap length, the calculated peak energy is larger than the experimental values, which may partly be attributed to molecular adsorbates that are not accounted for in the calculation. In addition, the facet width used in our calculation (12.5 nm) may be smaller than the actual dimension, and the resonance energy is expected to decrease with increasing facet width. 34,41 As the spacer thickness decreases, the calculated peak energy decreases rapidly, crossing the experimental trend line at  $d \sim 7$  nm and diverging to the infrared region. Overall, the average peak energy determined from our experiment shifts at a slower rate than the classical prediction. However, it is interesting to note that the spectral red-shifting and linewidth narrowing continues as the ALD oxide growth cycles are decreased to 4C which is expected to yield a spacer thickness smaller than 0.5 nm. This observation is in contrast to the relative blue-shift expected due to electron nonlocal screening and Landau damping effects that reduce the capacitive coupling strength. By fitting a biexponential function ( $E = E_0 - a_1 e^{-d/d_1} - a_2 e^{-d/d_2}$ , where Eand  $E_0$  are the resonance energies at gap length d and infinite particle-film separation, respectively, and  $d_1$  and  $d_2$  are decay lengths) to the experimental data points in Figure 3c, the resonance decay rates can be estimated as  $1/d_1 = 8.2 \text{ nm}^{-1}$  and  $1/d_2 = 0.2 \text{ nm}^{-1}$ . Similar fitting to the calculated values yields 0.7 and 0.2 nm<sup>-1</sup> decay rates. While the experimental decay rates depend on determining the d values accurately, it is clear that the red-shifting and spectral narrowing appear to be accelerated rather than slowing as the gap length approaches the quantum tunneling limit.

The accelerated red-shifting is accompanied by linewidth narrowing as can be seen comparing the trends in Figure 3b,c. Narrowing of plasmon resonances of a nanoparticle coupled to a metal film is expected based on the principles of classical electromagnetics due to hybridization of dipolar and quadrupolar plasmon modes. Here, the surprising observation is that the narrowing effect continues as the particle—film separation shrinks to the quantum tunneling limit. The spectral narrowing observed for the AuNR—AuF plasmonic systems is in contrast to the broadening expected in dimers of small nanoparticles due to enhanced rate of surface collision induced plasmon damping that increases with decreasing gap size. The nonlocal effect and surface collision plasmon damping

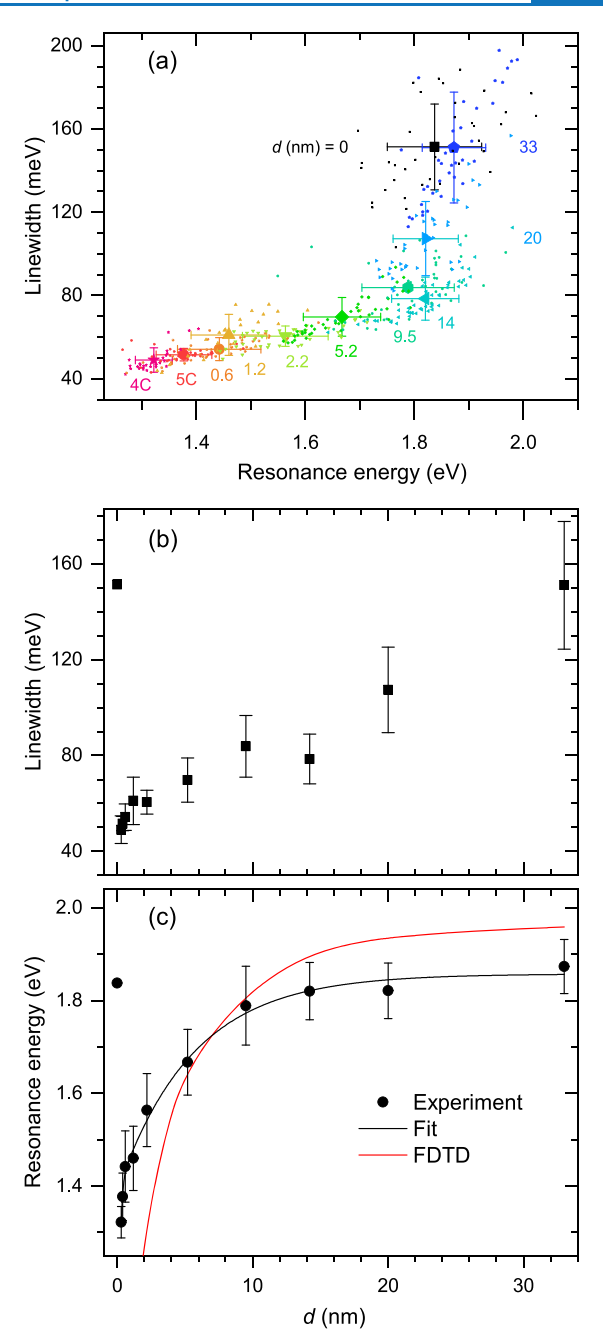


Figure 3. Plasmon resonance energy and linewidth extracted from single particle spectra by fitting the Lorentzian function to the experimental data. (a) Linewidth plotted as a function of the resonance energy. The small symbols represent the values extracted from the spectra of individual AuNRs coupled to the AuF at different d indicated on the plot. The large symbols are average values, and the error bars (one standard deviation) indicate the fluctuation from nanorod to nanorod. (b) Average linewidth as a function of d. (c) Average resonance energy (black circles) as a function of d compared to results of FDTD simulation (red line). The black solid line is biexponential functions fitted to experimental data (see text).

reduce the maximum field enhancement that can be attained in the sub-nanometer gap. <sup>12,13</sup> However, the reduction of the optical field enhancement in sub-nanometer gaps due to surface collision becomes less drastic with increasing size of the nanoparticles. <sup>13</sup> It appears that, for AuNRs coupled to AuF, the surface collision plasmon damping is less significant than expected in dimers of nanoparticles possibly because of the

relatively large effective mode volume as well as the superior optical quality of the AuNRs compared to spherical nanoparticles.<sup>36</sup> The cavity resonances of the AuNR-AuF plasmonic system can have different properties from that of the dipole-dipole coupling. For example, at the narrowest gap, the quality factor (the average peak energy divided by the average linewidth) is ~27, compared to ~15 for a silver nanosphere on gold film.<sup>33</sup> The large value of the quality factor indicates that photons can be confined in the AuNR-AuF cavity for a relatively long time.

#### APPEARANCE OF HIGH ORDER MODES

The spectral red-shifting and sharpening of the capacitive gap plasmon resonance with decreasing gap length are accompanied by weakening of scattering intensity. As the relatively sharp peaks in the near-infrared region weaken and vanish, broad resonances that have very weak scattering intensity start to appear in the visible spectral region. We note that the observation of different spectra for different AuNRs starting at 4C can be attributed to the nonuniformity of the oxide thickness at such a small number of growth cycles as mentioned earlier. The spectra indicated by the red lines in Figures 4a-c show that the sharp gap plasmon resonances further shift to the near-infrared region as the ALD cycles decreases from 5C to 4C and 3C. The spectra shown by the violet line reveal multiple high order cavity mode resonances as shown in Figure 4b-e and Figure S9. In the calculated spectra, signatures of high order modes are apparent starting at d = 5nm (see Figure S5). Their experimental observation appears to depend on the specific excitation and detection setups. For example, using all the pixels of the CCD camera of the spectrometer as opposed to the center one pixel enhances the relative signal intensity of higher order modes as demonstrated in Figure S10. In general, it appears that the scattering spectra shown by the violet lines that show multiple cavity modes (Figure 4 and Figure S9) can be induced by strong capacitive coupling, in line with past experimental observations<sup>33</sup> and theoretical analysis. 41 However, high order modes can also be induced due to conductive coupling, 43-45 and hence, they may not be unique spectral features to indicate the transition from capacitive to charge transfer interaction. When the oxide growth cycle is further reduced, in addition to the higher order multiple peaks, broad resonances with single peaks and stronger scattering intensity start to appear as indicated by the black lines in Figure 4c-e and Figure S9. Interestingly, the peak energies and linewidths of the broad resonances are within the range obtained in the absence of the ALD layer (d =0), where direct physical contact between the AuNR and the AuF can be assumed because the surface ligand on the colloidal AuNRs (cetyltrimethylammonium bromide, CTAB) does not provide complete electrical insulation due to nonuniform surface coverage.<sup>37</sup> In the FDTD simulations, broad resonances appear in the 2.25-2.13 eV energy range for d = 5-1 nm as can be seen in the normalized spectra in Figure S7. The fact that the peak energy is insensitive to the gap size indicates that the high energy resonance is due to the transverse mode of the rod. We note that the lowest calculated peak energy (2.13 eV) is higher than the highest experimentally observed peak energy that ranges from 1.64 to 2.02 eV.

To explain the observed spectral evolution with diminishing thickness of aluminum oxide, we have performed FDTD simulations by adding conductivity to the oxide as well as by

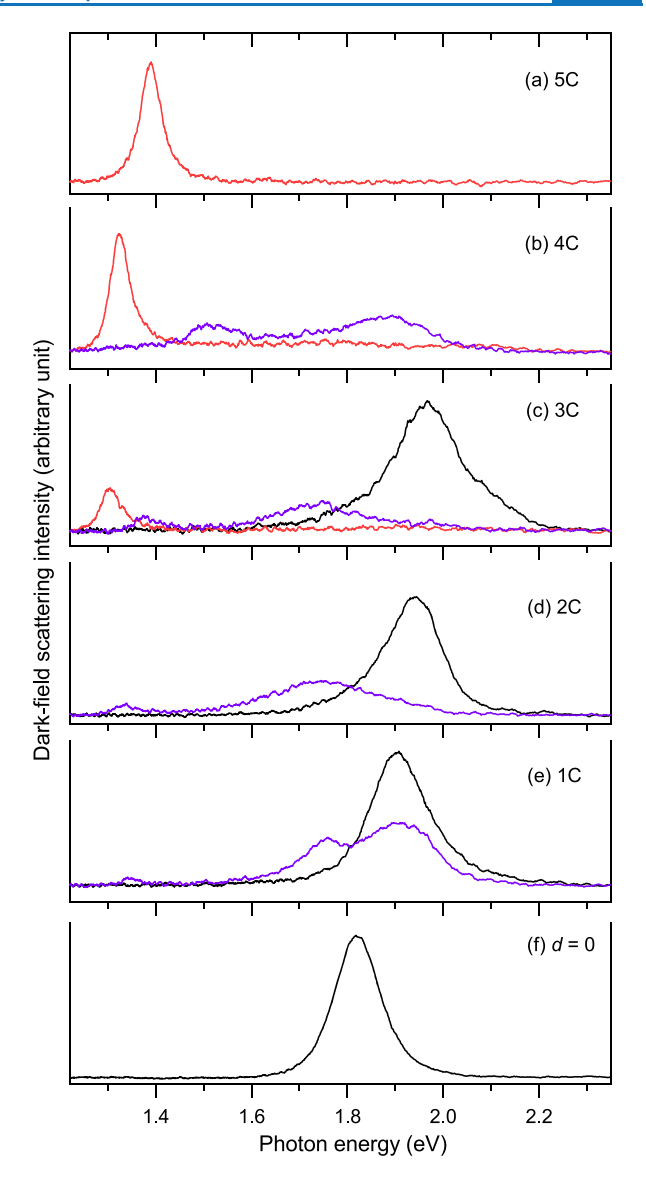


**Figure 4.** Scattering properties of AuNR on AuF at the spacer thickness obtained using 5C-0 ALD cycles. (a) For 5C, the scattering spectra are dominated by single peak resonances that appear in the near-infrared region. (b) For 4C ALD cycles, the single peak resonances (red line) shift further to the red, and multipeak resonances (violet lines) appear at higher energy. (c) At 3C, single peak resonances (red line) become rare, while the higher order modes (violet line) dominate, and signatures of tunneling and direct contact interaction start to appear (black line). At 2C (d) and 1C (e) ALD cycles, both the violet and black spectra become prevalent. (f) For the AuNR placed directly on the AuF, only the black spectra are observed, with average peak energy centered at  $1.84 \pm 0.09$  eV.

considering metal contact points. The conductivity  $(\sigma)$  is added by modifying the dielectric function  $(\varepsilon)$  of the oxide as  $\varepsilon=3.1+i\sigma\lambda/(2\pi\varepsilon_0c)$ , where  $\varepsilon_0$  is the permittivity of vacuum, c is the speed of light, and  $\lambda$  is the wavelength of light. The results for 3 nm spacing with conductivity are shown in Figure 5a (similar results are shown for 1 nm spacing in Figure S11). Figure 5a shows that the scattering cross-section of the dipolar gap plasmon resonance at 1.43 eV decreases with increasing conductivity and disappears completely at  $\sigma=5\times10^4~\Omega^{-1}$  m<sup>-1</sup>. At the same time, the small high order peaks are smoothed out while the peak at ~2.25 eV broadens and slightly red-shifts when  $\sigma$  is increased from  $1\times10^4$  to  $5\times10^4$ 

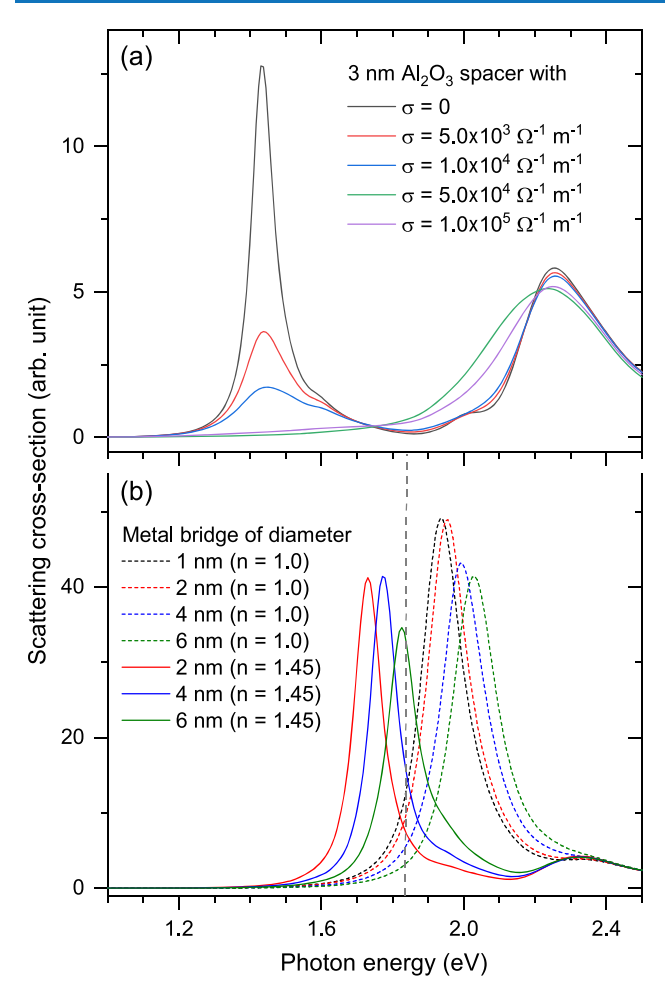


**Figure 5.** Spectral evolution upon increasing conductivity of the spacer layer. (a) The dipolar gap plasmon resonance at 1.43 eV disappears as the conductivity of the spacer between the AuNR and the AuF increases. (b) Effect of the cylindrical gold bridge with different diameters when the refractive index of the gap is n=1 (dashed lines) and n=1.45 (solid lines). In a given medium, increasing the diameter of the bridge results in blue-shifting of the peak position.

 $\Omega^{-1}$  m<sup>-1</sup>. A further increase of the conductivity shifts the peak position to the blue, which means that tuning the conductivity does not explain the range of peak positions (1.64–2.02 eV) observed experimentally. On the other hand, the peak position in the simulation can be tuned broadly by introducing a cylindrical metal bridge as shown in Figure 5b. The peak positions obtained in the presence of metal contact points can further be tuned by varying the refractive index of the interface. We note that the metal bridges account for direct AuNR–AuF contact points because of the nonuniformities of surface coverage of the AuNRs with CTAB<sup>49,50</sup> and the AuF with aluminum oxide as well as the roughness of the film. The dielectric spacing obtained using the aluminum oxide refers to the minimum particle—film separation, presumably at a point where there is no CTAB.

In Figure 5a,b, the dipolar gap plasmon resonance in the near-infrared region disappears due to conductive particle—film interaction, suggesting that it is an excellent ruler for indicating the nature of the particle—film interaction. The aluminum oxide spacer thickness obtained at 4C may provide a minimum gap size smaller than 0.5 nm as can be estimated based on the

trend observed in Figure 1c. At this gap size, electron tunneling through the dielectric spacer may be expected. According to the analysis of gold—vacuum—gold electrodes by Teague, <sup>47</sup> for tunneling to take place the vacuum spacing has to be smaller than 0.25 nm, which is comparable to the interplanar spacing in gold crystals.<sup>48</sup> This tunneling gap length is also in reasonable agreement with the results of a recent theoretical and experimental analysis.<sup>49,50</sup> However, for a nonvacuum medium, the tunneling barrier height depends on the molecular and dielectric properties of the interface.<sup>51</sup> In general, it is clear that the sharpening and narrowing of the dipolar gap plasmon resonance of the AuNR—AuF plasmonic system continue until it vanishes at the tunneling and conductive limit.

We note that the spectral evolutions observed in the subnanometer gap regime for the AuNRs coupled to AuF is not obvious when spherical gold nanoparticles are coupled to AuF. For gold nanospheres on AuF, the plasmon resonance energy monotonically shifts to the red, merging to the touching limit charge transfer plasmon resonance energy that peaks on average at ~1.8 eV as shown in Figure S12 for the coupling of 100 nm diameter gold spheres to gold film. The trend observed in Figure S12 agrees with published data that show continuous red-shifting of peak energy when the aluminum oxide spacer thickness between 60 nm gold spheres and gold film decreases.<sup>20</sup> In agreement with the experimental observations, the results of the FDTD simulations presented in Figure S13a indicate that the sharp resonance of the rod-film system is excited with in-plane polarized light, while out-of-plane polarization is needed for exciting the sphere-film system. That is, the vertical polarization that is most favorable for coupling the excitation of the sphere to the film is least favorable for exciting the cavity resonance of the rod-film system as can be seen comparing the results in Figure S13a,b. This confirms that the sharp resonances observed for the AuNR-AuF plasmonic system in our experiment are due to cavity mode resonances that have a different excitation mechanism from the excitation of the nanosphere on metal film that couples through dipole-image dipole interaction.

In summary, by varying the dielectric spacing between gold nanorods and gold film from over 30 nm to the touching limit, a complete picture of plasmon coupling is provided. In contrast to the nonlocal, quantum mechanical, and Landau damping effects that induce relative spectral blue-shifting and broadening, continuous peak energy red-shifting and linewidth narrowing are observed apparently up to the tunneling limit. The experimental results presented here suggest that as the red-shifted sharp gap plasmon resonances vanish at the quantum tunneling limit, high order cavity modes takes precedence. With the gap length decreasing to the direct contact limit, the resonances converge to a single peak charge transfer plasmon resonance that appear at ~1.8 eV, regardless of particle size. The results presented here provide a clear picture for the properties of gap plasmon resonances as the coupling interaction transitions from capacitive to charge transfer and may facilitate the development of improved theoretical modeling.

### ASSOCIATED CONTENT

# Supporting Information

The Supporting Information is available free of charge at https://pubs.acs.org/doi/10.1021/acsphotonics.0c00225.

Description of sample fabrication, preparation, and analysis as well as supporting figures including AFM images, FDTD simulation results, field distribution and polarization, schematics, extinction vs photon energy, dependence of peak cross-section on collection angle, normalized scattering cross-sections, evolution of AuNR-AuF gap plasmon resonances, and dark-field scattering intensity (PDF)

#### AUTHOR INFORMATION

#### **Corresponding Author**

Terefe G. Habteyes — Center for High Technology Materials and Department of Chemistry and Chemical Biology, University of New Mexico, Albuquerque, New Mexico 87131, United States; orcid.org/0000-0001-5978-6464; Email: habteyes@unm.edu

#### **Authors**

Sharmin Haq — Center for High Technology Materials, University of New Mexico, Albuquerque, New Mexico 87131, United States

**Tefera E. Tesema** — Center for High Technology Materials and Department of Chemistry and Chemical Biology, University of New Mexico, Albuquerque, New Mexico 87131, United States

Bisweswar Patra — Center for High Technology Materials, University of New Mexico, Albuquerque, New Mexico 87131, United States

Eric Gomez — Center for High Technology Materials, University of New Mexico, Albuquerque, New Mexico 87131, United States

Complete contact information is available at: https://pubs.acs.org/10.1021/acsphotonics.0c00225

#### **Author Contributions**

§S.H. and T.E.T. contributed equally. The manuscript was written through contributions of all authors. All authors have given approval to the final version of the manuscript.

#### **Notes**

The authors declare no competing financial interest.

# ACKNOWLEDGMENTS

This research has been supported by the U.S. National Science Foundation Grant 1651478 and the U.S. Air Force Office of Scientific Research Grant FA9550-18-1-0512. This work was performed, in part, at the Center for Integrated Nanotechnologies (CINT), an Office of Science User Facility operated for the U.S. Department of Energy (DOE) Office of Science by Los Alamos National Laboratory (Contract DE-AC52-06NA25396) and Sandia National Laboratories (Contract DE-NA-0003525). We thank Dr. Igal Brener for facilitating our access to CINT, and Prof. Alejandro Manjavacas and Dr. Stavroula Foteinopoulou for the helpful discussion during the initial phase of the electromagnetic simulation.

## REFERENCES

- (1) Hao, E.; Schatz, G. C. Electromagnetic Fields around Silver Nanoparticles and Dimers. J. Chem. Phys. **2004**, 120 (1), 357–366.
- (2) Kneipp, K.; Moskovits, M.; Kneipp, H. Topics in Applied Physics; Springer: Germany, 2006; Vol. 103.
- (3) Romero, I.; Aizpurua, J.; Bryant, G. W.; de Abajo, F. J. G. Plasmons in Nearly Touching Metallic Nanoparticles: Singular

Response in the Limit of Touching Dimers. Opt. Express 2006, 14 (21), 9988-9999.

- (4) Zuloaga, J.; Prodan, E.; Nordlander, P. Quantum Description of the Plasmon Resonances of a Nanoparticle Dimer. *Nano Lett.* **2009**, 9 (2), 887–891.
- (5) Esteban, R.; Borisov, A. G.; Nordlander, P.; Aizpurua, J. Bridging Quantum and Classical Plasmonics with a Quantum-Corrected Model. *Nat. Commun.* **2012**, *3*, 825.
- (6) Christensen, T.; Yan, W.; Jauho, A. P.; Soljacic, M.; Mortensen, N. A. Quantum Corrections in Nanoplasmonics: Shape, Scale, and Material. *Phys. Rev. Lett.* **2017**, *118* (15), 157402.
- (7) Savage, K. J.; Hawkeye, M. M.; Esteban, R.; Borisov, A. G.; Aizpurua, J.; Baumberg, J. J. Revealing the Quantum Regime in Tunnelling Plasmonics. *Nature* **2012**, 491 (7425), 574–577.
- (8) Ciraci, C.; Hill, R. T.; Mock, J. J.; Urzhumov, Y.; Fernandez-Dominguez, A. I.; Maier, S. A.; Pendry, J. B.; Chilkoti, A.; Smith, D. R. Probing the Ultimate Limits of Plasmonic Enhancement. *Science* **2012**, 337 (6098), 1072–1074.
- (9) Scholl, J. A.; Garcia-Etxarri, A.; Koh, A. L.; Dionne, J. A. Observation of Quantum Tunneling between Two Plasmonic Nanoparticles. *Nano Lett.* **2013**, *13* (2), 564–569.
- (10) Zhu, W. Q.; Crozier, K. B. Quantum Mechanical Limit to Plasmonic Enhancement as Observed by Surface-Enhanced Raman Scattering. *Nat. Commun.* **2014**, *5*, 5228.
- (11) Zhu, W. Q.; Esteban, R.; Borisov, A. G.; Baumberg, J. J.; Nordlander, P.; Lezec, H. J.; Aizpurua, J.; Crozier, K. B. Quantum Mechanical Effects in Plasmonic Structures with Subnanometre Gaps. *Nat. Commun.* **2016**, *7*, 11495.
- (12) García de Abajo, F. J. Nonlocal Effects in the Plasmons of Strongly Interacting Nanoparticles, Dimers, and Waveguides. *J. Phys. Chem. C* **2008**, *112* (46), 17983–17987.
- (13) Khurgin, J.; Tsai, W. Y.; Tsai, D. P.; Sun, G. Landau Damping and Limit to Field Confinement and Enhancement in Plasmonic Dimers. ACS Photonics 2017, 4 (11), 2871–2880.
- (14) Mock, J. J.; Hill, R. T.; Degiron, A.; Zauscher, S.; Chilkoti, A.; Smith, D. R. Distance-Dependent Plasmon Resonant Coupling between a Gold Nanoparticle and Gold Film. *Nano Lett.* **2008**, 8 (8), 2245–2252.
- (15) Li, G. C.; Zhang, Q.; Maier, S. A.; Lei, D. Plasmonic Particle-on-Film Nanocavities: A Versatile Platform for Plasmon-Enhanced Spectroscopy and Photochemistry. *Nanophotonics* **2018**, 7 (12), 1865–1889.
- (16) Hill, R. T.; Mock, J. J.; Hucknall, A.; Wolter, S. D.; Jokerst, N. M.; Smith, D. R.; Chilkoti, A. Plasmon Ruler with Angstrom Length Resolution. *ACS Nano* **2012**, *6* (10), 9237–9246.
- (17) Mertens, J.; Eiden, A. L.; Sigle, D. O.; Huang, F. M.; Lombardo, A.; Sun, Z. P.; Sundaram, R. S.; Colli, A.; Tserkezis, C.; Aizpurua, J.; Milana, S.; Ferrari, A. C.; Baumberg, J. J. Controlling Subnanometer Gaps in Plasmonic Dimers Using Graphene. *Nano Lett.* **2013**, *13* (11), 5033–5038.
- (18) Liu, D. J.; Wu, T. T.; Zhang, Q.; Wang, X. M.; Guo, X. Y.; Su, Y. K.; Zhu, Y.; Shao, M. H.; Chen, H. J.; Luo, Y.; Lei, D. Y. Probing the in-Plane near-Field Enhancement Limit in a Plasmonic Particle-on-Film Nanocavity with Surface-Enhanced Raman Spectroscopy of Graphene. ACS Nano 2019, 13 (7), 7644–7654.
- (19) Chikkaraddy, R.; Turek, V. A.; Kongsuwan, N.; Benz, F.; Carnegie, C.; van de Goor, T.; de Nijs, B.; Demetriadou, A.; Hess, O.; Keyser, U. F.; Baumberg, J. J. Mapping Nanoscale Hotspots with Single-Molecule Emitters Assembled into Plasmonic Nanocavities Using DNA Origami. *Nano Lett.* **2018**, *18* (1), 405–411.
- (20) Ciraci, C.; Chen, X. S.; Mock, J. J.; McGuire, F.; Liu, X. J.; Oh, S. H.; Smith, D. R. Film-Coupled Nanoparticles by Atomic Layer Deposition: Comparison with Organic Spacing Layers. *Appl. Phys. Lett.* **2014**, *104* (2), No. 023109.
- (21) Chen, W.; Zhang, S. P.; Deng, Q.; Xu, H. X. Probing of Sub-Picometer Vertical Differential Resolutions Using Cavity Plasmons. *Nat. Commun.* **2018**, *9*, 801.
- (22) Benz, F.; Tserkezis, C.; Herrmann, L. O.; de Nijs, B.; Sanders, A.; Sigle, D. O.; Pukenas, L.; Evans, S. D.; Aizpurua, J.; Baumberg, J. J.

- Nanooptics of Molecular-Shunted Plasmonic Nanojunctions. *Nano Lett.* **2015**, *15* (1), 669–674.
- (23) Cui, X. M.; Qin, F.; Lai, Y. H.; Wang, H.; Shao, L.; Chen, H. J.; Wang, J. F.; Lin, H. Q. Molecular Tunnel Junction-Controlled High-Order Charge Transfer Plasmon and Fano Resonances. *ACS Nano* **2018**, *12* (12), 12541–12550.
- (24) Choi, H.-K.; Park, W.-H.; Park, C.-G.; Shin, H.-H.; Lee, K. S.; Kim, Z. H. Metal-Catalyzed Chemical Reaction of Single Molecules Directly Probed by Vibrational Spectroscopy. *J. Am. Chem. Soc.* **2016**, *138* (13), 4673–4684.
- (25) Park, W.-H.; Kim, Z. H. Charge Transfer Enhancement in the Sers of a Single Molecule. *Nano Lett.* **2010**, *10* (10), 4040–4048.
- (26) Benz, F.; Schmidt, M. K.; Dreismann, A.; Chikkaraddy, R.; Zhang, Y.; Demetriadou, A.; Carnegie, C.; Ohadi, H.; de Nijs, B.; Esteban, R.; Aizpurua, J.; Baumberg, J. J. Single-Molecule Optomechanics in "Picocavities". *Science* **2016**, 354 (6313), 726–729.
- (27) Hu, M.; Ghoshal, A.; Marquez, M.; Kik, P. G. Single Particle Spectroscopy Study of Metal-Film-Induced Tuning of Silver Nanoparticle Plasmon Resonances. *J. Phys. Chem. C* **2010**, *114* (16), 7509–7514.
- (28) Chen, S. Y.; Mock, J. J.; Hill, R. T.; Chilkoti, A.; Smith, D. R.; Lazarides, A. A. Gold Nanoparticles on Polarizable Surfaces as Raman Scattering Antennas. *ACS Nano* **2010**, *4* (11), 6535–6546.
- (29) Yamamoto, N.; Ohtani, S.; de Abajo, F. J. G. Gap and Mie Plasmons in Individual Silver Nanospheres near a Silver Surface. *Nano Lett.* **2011**, *11* (1), 91–95.
- (30) Lei, D. Y.; Fernandez-Dominguez, A. I.; Sonnefraud, Y.; Appavoo, K.; Haglund, R. F.; Pendry, J. B.; Maier, S. A. Revealing Plasmonic Gap Modes in Particle-on-Film Systems Using Dark-Field Spectroscopy. *ACS Nano* **2012**, *6* (2), 1380–1386.
- (31) Mock, J. J.; Hill, R. T.; Tsai, Y. J.; Chilkoti, A.; Smith, D. R. Probing Dynamically Tunable Localized Surface Plasmon Resonances of Film-Coupled Nanoparticles by Evanescent Wave Excitation. *Nano Lett.* **2012**, *12* (4), 1757–1764.
- (32) Ha, J. W.; Marchuk, K.; Fang, N. Focused Orientation and Position Imaging (Fopi) of Single Anisotropic Plasmonic Nanoparticles by Total Internal Reflection Scattering Microscopy. *Nano Lett.* **2012**, *12* (8), 4282–4288.
- (33) Chikkaraddy, R.; Zheng, X. Z.; Benz, F.; Brooks, L. J.; de Nijs, B.; Carnegie, C.; Kleemann, M. E.; Mertens, J.; Bowman, R. W.; Vandenbosch, G. A. E.; Moshchalkov, V. V.; Baumbere, J. J. How Ultranarrow Gap Symmetries Control Plasmonic Nanocavity Modes: From Cubes to Spheres in the Nanoparticle-on-Mirror. *ACS Photonics* **2017**, *4* (3), 469–475.
- (34) Huh, J. H.; Lee, J.; Lee, S. Comparative Study of Plasmonic Resonances between the Roundest and Randomly Faceted Au Nanoparticles-on-Mirror Cavities. *ACS Photonics* **2018**, *5* (2), 413–421.
- (35) Zhang, Q.; Li, G. C.; Lo, T. W.; Lei, D. Y. Polarization-Resolved Optical Response of Plasmonic Particle-on-Film Nanocavities. *J. Opt.* **2018**, *20* (2), No. 024010.
- (36) Sonnichsen, C.; Franzl, T.; Wilk, T.; von Plessen, G.; Feldmann, J.; Wilson, O.; Mulvaney, P. Drastic Reduction of Plasmon Damping in Gold Nanorods. *Phys. Rev. Lett.* **2002**, 88 (7), No. 077402.
- (37) Kafle, B.; Gieri, P.; Kookhaee, H.; Tesema, T. E.; Haq, S.; Manjavacas, A.; Habteyes, T. G. Robust Charge Transfer Plasmons in Metallic Particle—Film Systems. *ACS Photonics* **2018**, *5* (10), 4022—4029.
- (38) Whitney, A. V.; Elam, J. W.; Zou, S. L.; Zinovev, A. V.; Stair, P. C.; Schatz, G. C.; Van Duyne, R. P. Localized Surface Plasmon Resonance Nanosensor: A High-Resolution Distance-Dependence Study Using Atomic Layer Deposition. *J. Phys. Chem. B* **2005**, *109* (43), 20522–20528.
- (39) Filter, R.; Qi, J.; Rockstuhl, C.; Lederer, F. Circular Optical Nanoantennas: An Analytical Theory. *Phys. Rev. B: Condens. Matter Mater. Phys.* **2012**, *85* (12), 125429.

- (40) Minkowski, F.; Wang, F.; Chakrabarty, A.; Wei, Q. H. Resonant Cavity Modes of Circular Plasmonic Patch Nanoantennas. *Appl. Phys. Lett.* **2014**, *104* (2), No. 021111.
- (41) Tserkezis, C.; Esteban, R.; Sigle, D. O.; Mertens, J.; Herrmann, L. O.; Baumberg, J. J.; Aizpurua, J. Hybridization of Plasmonic Antenna and Cavity Modes: Extreme Optics of Nanoparticle-on-Mirror Nanogaps. *Phys. Rev. A: At., Mol., Opt. Phys.* **2015**, 92 (5), No. 053811.
- (42) Sobhani, A.; Manjavacas, A.; Cao, Y.; McClain, M. J.; de Abajo, F. J.; Nordlander, P.; Halas, N. J. Pronounced Linewidth Narrowing of an Aluminum Nanoparticle Plasmon Resonance by Interaction with an Aluminum Metallic Film. *Nano Lett.* **2015**, *15* (10), 6946–6951
- (43) Atay, T.; Song, J. H.; Nurmikko, A. V. Strongly Interacting Plasmon Nanoparticle Pairs: From Dipole-Dipole Interaction to Conductively Coupled Regime. *Nano Lett.* **2004**, *4* (9), 1627–1631.
- (44) Lassiter, J. B.; Aizpurua, J.; Hernandez, L. I.; Brandl, D. W.; Romero, I.; Lal, S.; Hafner, J. H.; Nordlander, P.; Halas, N. J. Close Encounters between Two Nanoshells. *Nano Lett.* **2008**, 8 (4), 1212–1218.
- (45) Habteyes, T. G.; Dhuey, S.; Cabrini, S.; Schuck, P. J.; Leone, S. R. Theta-Shaped Plasmonic Nanostructures: Bringing "Dark" Multipole Plasmon Resonances into Action Via Conductive Coupling. *Nano Lett.* **2011**, *11* (4), 1819–1825.
- (46) Hajisalem, G.; Min, Q.; Gelfand, R.; Gordon, R. Effect of Surface Roughness on Self-Assembled Monolayer Plasmonic Ruler in Nonlocal Regime. *Opt. Express* **2014**, 22 (8), 9604–9610.
- (47) Teague, E. C. Room-Temperature Gold-Vacuum-Gold Tunneling Experiments. J. Res. Natl. Bur. Stand. 1986, 91 (4), 171–233.
- (48) Davey, W. P. Precision Measurements of the Lattice Constants of Twelve Common Metals. *Phys. Rev.* **1925**, *25* (6), 753–761.
- (49) Aguirregabiria, G.; Marinica, D. C.; Esteban, R.; Kazansky, A. K.; Aizpurua, J.; Borisov, A. G. Role of Electron Tunneling in the Nonlinear Response of Plasmonic Nanogaps. *Phys. Rev. B: Condens. Matter Mater. Phys.* **2018**, 97 (11), 115430.
- (50) Zhang, Q.; Cai, X.; Yu, X.; Carregal-Romero, S.; Parak, W. J.; Sachan, R.; Cai, Y.; Wang, N.; Zhu, Y.; Lei, D. Y. Electron Energy-Loss Spectroscopy of Spatial Nonlocality and Quantum Tunneling Effects in the Bright and Dark Plasmon Modes of Gold Nanosphere Dimers. Adv. Quantum Technol. 2018, 1, 1800016.
- (51) Tan, S. F.; Wu, L.; Yang, J. K. W.; Bai, P.; Bosman, M.; Nijhuis, C. A. Quantum Plasmon Resonances Controlled by Molecular Tunnel Junctions. *Science* **2014**, *343* (6178), 1496–1499.